Computers in Biology and Medicine 135 (2021) 104547

Contents lists available at ScienceDirect

Computers in Biology and Medicine

journal homepage: www.elsevier.com/locate/compbiomed

Predicting cell behaviour parameters from glioblastoma on a chip images. A deep learning approach

Marina Pérez-Aliacar [a,b], Mohamed H. Doweidar [a,b,d], Manuel Doblaré [a,c,d], Jacobo Ayensa-Jiménez [a,b,c,*]

[a] Aragon Institute of Engineering Research (I3A), University of Zaragoza, Mariano Esquillor S/N, Zaragoza, Spain
[b] Mechanical Engineering Department, University of Zaragoza, María de Luna S/N, Zaragoza, Spain
[c] Aragon Institute of Health Research (IIS Aragón), University of Zaragoza, San Juan Bosco 13, Zaragoza, Spain
[d] Centro de Investigación Biomédica en Red en Bioingeniería, Biomateriales y Nanomedicina (CIBER-BBN), Monforte de Lemos 3-5, Pabellón 11. Planta 0, Madrid, Spain

ARTICLE INFO

Keywords:
Intelligent microfluidics
Deep learning
Glioblastoma
Identification of biological parameters

ABSTRACT

The broad possibilities offered by microfluidic devices in relation to massive data monitoring and acquisition open the door to the use of deep learning technologies in a very promising field: cell culture monitoring. In this work, we develop a methodology for parameter identification in cell culture from fluorescence images using Convolutional Neural Networks (CNN). We apply this methodology to the *in vitro* study of glioblastoma (GBM), the most common, aggressive and lethal primary brain tumour. In particular, the aim is to predict the three parameters defining the *go or grow* GBM behaviour, which is determinant for the tumour prognosis and response to treatment. The data used to train the network are obtained from a mathematical model, previously validated with *in vitro* experimental results. The resulting CNN provides remarkably accurate predictions (Pearson's $\rho >$ 0.99 for all the parameters). Besides, it proves to be sound, to filter noise and to generalise. After training and validation with synthetic data, we predict the parameters corresponding to a real image of a microfluidic experiment. The obtained results show good performance of the CNN. The proposed technique may set the first steps towards patient-specific tools, able to predict in real-time the tumour evolution for each particular patient, thanks to a combined *in vitro-in silico* approach.

1. Introduction

According to the World Health Organization, cancer is the second leading cause of death in the world, responsible for about 10 million deaths per year. These figures are expected to rise to 16 million deaths in 2040. Approximately one sixth of the total number of deaths are due to cancer. Among the more than 200 types of cancer, Glioblastoma (GBM) is the most aggressive and frequent primary brain tumour, accounting for 17% of these tumours [14]. Survival of GBM patients who undergo the first-line standard treatments (surgery followed by adjuvant chemotherapy and local radiation) has a median of 14 months since diagnosis and a 5-year survival rate of only 6.8% [47,48]. This is due to its heterogeneity, rapid progression and high invasive capacity [23,24].

Hypoxia has been proposed as one of the main driving forces of GBM progression [15]. GBM cells proliferate around blood vessels, eventually provoking their occlusion, leading to local hypoxia. As a consequence, many cells die in this hypoxic region, forming a necrotic core around the collapsed vessel, while the surviving cells rapidly migrate towards more oxygenated areas, creating waves with high cellular density, called pseudopalisades. Once they reach a new vessel, they stop migrating and start a fast proliferation, so the whole process is restarted. As a result, cells undergo migration and proliferation cycles, in a dichotomous process known as *go or grow*, which proposes that cells exhibit either a migratory or proliferative state depending on the oxygen level [31]. It is therefore clear that characterising the *go or grow* paradigm in GBM behaviour is key for the development of treatment strategies against this cancer [62], as it also plays a crucial role in the acquisition of chemo-resistance [38].

Due to the complexity of GBM evolution (and of cell biological processes in general), which strongly depends on the particular micro-environment [16], two-dimensional *in vitro* experiments (Petri dishes) are not able to reproduce the behaviour of cells in real tissues.

* Corresponding author. Aragon Institute of Engineering Research (I3A), University of Zaragoza, Mariano Esquillor S/N, Zaragoza, Spain.
E-mail addresses: marina.perez@unizar.es (M. Pérez-Aliacar), mohamed@unizar.es (M.H. Doweidar), mdoblare@unizar.es (M. Doblaré), jacoboaj@unizar.es (J. Ayensa-Jiménez).

https://doi.org/10.1016/j.compbiomed.2021.104547
Received 27 April 2021; Received in revised form 28 May 2021; Accepted 31 May 2021
Available online 6 June 2021

Microfluidics and micro-technologies have recently arisen as powerful tools to recreate the complex three-dimensional microenvironment that governs tumour dynamics [54], and, in particular, GBM [13], thus overcoming some of these limitations. These techniques allow to reproduce important characteristics of tumour evolution that were not observed before in two-dimensional cultures, as well as testing drugs in a much more efficient way [29,57]. In particular, the study of tumour chemotaxis has been considerably developed [46,59]. Besides, thanks to the flexibility, reproducibility, automation, integration and miniaturisation of microfluidic experiments, they have the potential to generate large amounts of data, in the form of images and videos of long periods of cell culture evolution [20]. This fact enables to use the framework of Data Science and, in particular, of Machine Learning methods to analyse these complex, multifactorial and very nonlinear biological problems.

The use of Machine Learning in Biomechanics and Bioengineering has been very fruitful in the last two decades (see for example Hosseini et al. [34], Caschera et al. [18], Halilaj et al. [30]). A very common application of Machine Learning and, in particular, of Neural Networks is as a Reduced Order Model built from Finite Element simulations [50]. This strategy can be oriented towards real time patient-specific tools (see, for instance, Cabeza-Gil et al. [17] for an application in ophthalmology). The use of Neural Networks is also very common for parameter identification or constitutive modelling in computational mechanics. Some examples, out of the huge amount, are soft tissues [5,19,41], history and rate dependent materials [2,3,25,37], granular materials [22,27,58,64] and polymeric, polycrystalline and composite materials [1,4,7,42,43]. Recently, Deep Convolutional Neural Networks (CNN) have emerged in computational mechanics [49,55,60,61] as powerful tools to exploit the information contained spatially in the datasets, as occurs in medical image processing [40,52,56].

The broad possibilities offered by microfluidic devices in relation to massive data monitoring and acquisition open the door to the use of deep learning technologies in a promising field: cell culture monitoring [26,53], which has been little explored. Very recently, some attempts have been made for classification problems [63] or feature extraction [33,35]. However, Neural Networks have not been applied, up to the authors' knowledge, to parameter identification in cell culture applications, being this a field that remains to be explored. Here, we present a Deep Learning approach that uses CNN for parameter identification in physically-based models of cell-cultures, from microscopic images of such cultures in microfluidic devices. This framework is then applied to discover important features of GBM cells during the formation of a necrotic core, thus helping to predict GBM evolution. The Neural Network is trained using synthetic data obtained from a validated mathematical model and considering a wide range of parameters. The presented methodology may then be considered as a first step towards personalized medicine, where each patient, with its own tumour characteristics and evolution, is *in vitro* evaluated to get their patient-specific parameters.

The paper is structured as follows. The methods are presented in Section 2. First, the procedures for image acquisition and processing from microfluidic devices are described. Then, the mathematical model, used to predict GBM evolution in microfluidic devices, is presented and the parameters associated with the *go or grow* behaviour (having a direct impact in tumour progression) are identified. Finally, the CNN framework and the details about the training process are described. Section 3 introduces the main results of the paper, in terms of the network performance and the model generalisation. The results are additionally validated with previously published results on GBM culture evolution, including a different experimental configuration from the one used for training. Finally, Section 4, presents a discussion about the methodology and Section 5 summarizes the main results and conclusions.

2. Materials and methods

2.1. Image processing

The outcome of cell culture microfluidic experiments are often fluorescence images. Fluorescence microscopy has become an essential tool in cell biology, allowing to visualise cells, tissues and organelles. In order to be suitable for this technique, samples must be fluorescent. This can be achieved transducing cells so that they express fluorescent proteins or using fluorescent dyes. In particular, in the images used in this work, calcein was used to stain alive cells green, and propidium iodide to stain dead cells red [12,13]. Cells were then excited to show either green or red fluorescence, two images were taken with a confocal microscopy and then superimposed to obtain the final image (Fig. 1, stage 1). Due to the importance of fluorescence microscopy images in current research, they will be the starting point of the methodology presented herein. Precisely, fluorescent images of GBM cells cultured in microfluidic devices will be used. These images are taken at a low magnification scale to consider the phenomena in the whole device, as we work at the population scale, much higher than the cell size. These images need then to be processed to obtain the cell concentration profiles, which will be the network input.

A scheme of the image processing procedure is depicted in Fig. 1, where the different stages are indicated with blue numbers. From the given image (Stage 1), obtained from Ref. [13], a rectangular region across the central microchamber of the device is selected (Stage 2). Next, we separate alive cells (marked with green fluorescence) and dead cells (marked with red fluorescence). The two resultant images contain the values of green and red intensity for each pixel, measured in the range [0, 255] (Stages 3 & 4). Gaussian filtering with $\sigma = 3$ is then performed (Stages 5 & 6) to get information on the cell population density, instead of counting individual cells, as our continuum model requires. Finally, to obtain a one-dimensional cell concentration profile, the color intensity level is averaged throughout the chip length (Stages 7 & 8). To transform the intensity levels $\boldsymbol{I}_{\text{green}}$, $\boldsymbol{I}_{\text{red}}$ into cell concentrations $\boldsymbol{C}_n$, $\boldsymbol{C}_d$, we assume linear proportionality between both magnitudes, so, we can write:

$$\kappa I_{\text{green}}(x,t) = C_n(x,t), \tag{1}$$

$$\kappa I_{\text{red}}(x,t) = C_d(x,t), \tag{2}$$

with κ the constant of proportionality. To calculate κ, we assume that the integral of the initial cell concentration along the chamber equals the total amount of seeded cells (which are only alive cells). That is

$$\int_0^L C_n(x, t=0)dx = C_0 L, \tag{3}$$

where L is the chip length and C_0 is the initial cell concentration, known by the experimentalist. Finally, joining Eqs. (1) and (3), κ is obtained as:

$$\kappa = \frac{C_0 L}{\int_0^L I_{\text{green}} dx}. \tag{4}$$

Once the value of κ is determined, we can determine both alive (from Eq. (1)) and dead (from Eq. (2)) cell concentration profiles from an image, taken at any given time, at each point of the microchamber (Stage 9).

2.2. Mathematical model for glioblastoma evolution

The main measurement variable in our problem is the cell concentration profile for alive and necrotic cell populations, $C_n(x)$, and $C_d(x)$, $x \in [0; L]$, respectively. We can model the time evolution of these variables by means of a recently published mathematical model based on an advection-diffusion-reaction system of partial differential equations [10]. This computational model has been validated with data corresponding to experimental GBM cell cultures in a microfluific device,

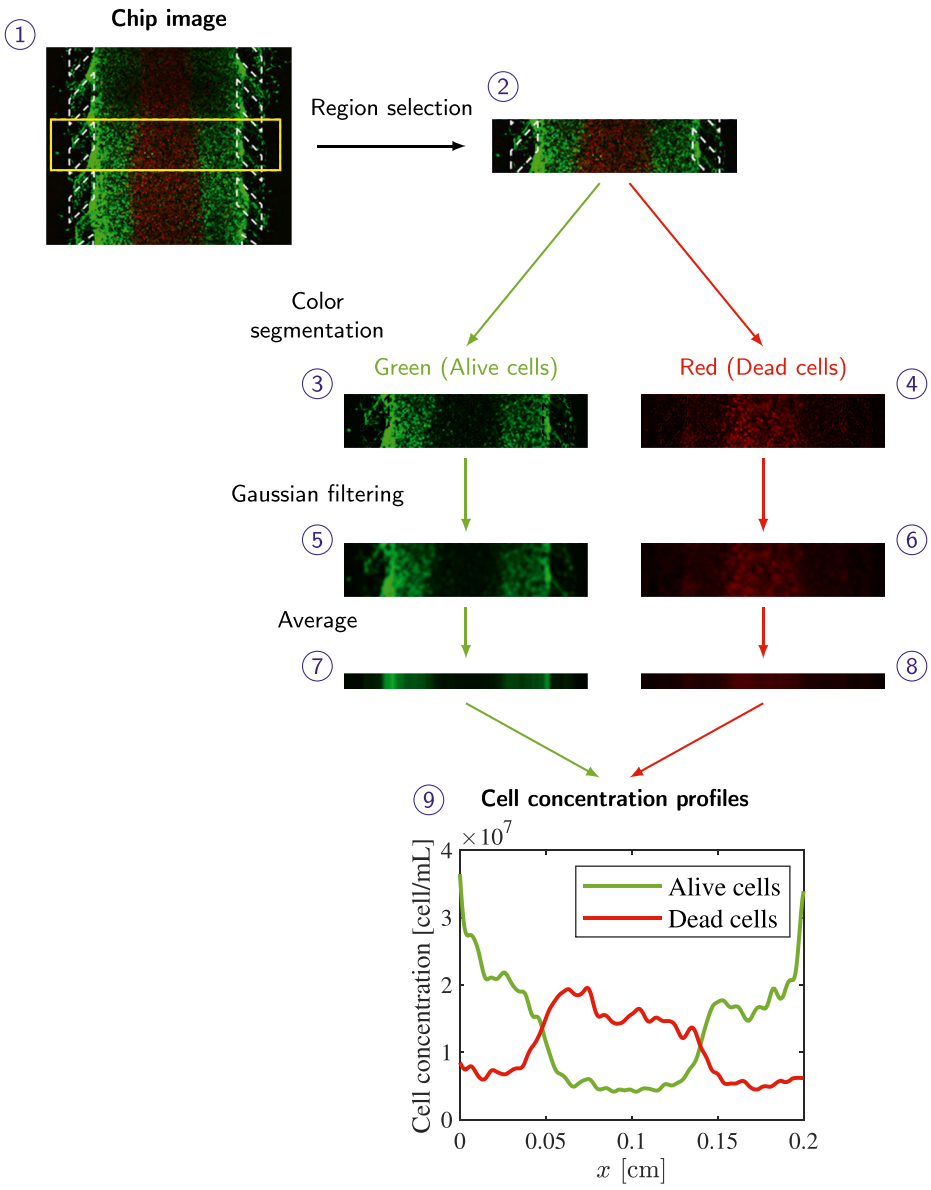

Fig. 1. Image processing procedure. The different stages are indicated with blue numbers. Fluorescence images from Ayensa-Jiménez et al. [10].

under hypoxic conditions, in different situations: the formation of a necrotic core [13], of a pseudopalisade [12] and of a double symmetric pseudopalisade [10].

The model governing equations, describing the evolution of both alive and dead cell concentrations (C_n, C_d) and of the oxygen concentration (O_2), are expressed as:

$$\frac{\partial C_n}{\partial t} = \frac{\partial}{\partial x}\left(D_n\frac{\partial C_n}{\partial x} - K_n\Pi_{ch}(O_2)F_{ch}(C_n)C_n\frac{\partial O_2}{\partial x}\right) + \frac{1}{\tau_{gr}}\Pi_{gr}(O_2)F_{gr}(C_n, C_d)C_n - \frac{1}{\tau_{ap}}F_{ap}(O_2)C_n, \tag{5}$$

$$\frac{\partial C_d}{\partial t} = \frac{1}{\tau_{ap}}F_{ap}(O_2)C_n, \tag{6}$$

$$\frac{\partial O_2}{\partial t} = D_{O_2}\frac{\partial^2 O_2}{\partial x^2} - \alpha_n F_c(O_2)C_n, \tag{7}$$

where Π_{ch}, F_{ch}, Π_{gr}, F_{gr}, F_{ap}, and F_c are nonlinear corrections accounting for different mechanisms of cell behaviour [10]. In particular, Π_{ch} and Π_{gr} define the *go or grow* behaviour of GBM cells [31,62]. The underlying assumption is that cells spend their resources either in proliferating or in migrating, depending on whether they are above or below a certain hypoxia threshold O_2^H.

$$\Pi_{ch}(O_2; O_2^H) = \begin{cases} 1 - O_2/O_2^H & \text{if} \quad 0 \le O_2 \le O_2^H \\ 0 & \text{if} \quad O_2 > O_2^H \end{cases}, \tag{8}$$

$$\Pi_{gr}(O_2; O_2^H) = \begin{cases} O_2/O_2^H & \text{if} \quad 0 \le O_2 \le O_2^H \\ 1 & \text{if} \quad O_2 > O_2^H \end{cases}. \tag{9}$$

Besides, F_{ch} is a chemotaxis correction accounting for cell concentration. Cells may migrate only when the cell concentration is below the saturation capacity C_{sat}. In the same way, F_{gr} is a logistic growth correction accounting for space and nutrients availability, decreasing growth as cell concentration approaches C_{sat}:

$$F_{ch}(C_n; C_{sat}) = \begin{cases} 1 - C_n/C_{sat} & \text{if} \quad 0 \le C_n \le C_{sat} \\ 0 & \text{if} \quad C_n > C_{sat} \end{cases}, \tag{10}$$

$$F_{gr}(C_n, C_d; C_{sat}) = \left(1 - \frac{C_n + C_d}{C_{sat}}\right) \tag{11}$$

Also, F_{ap} is a death activation function, incorporating both death mechanisms, necrosis due to hypoxia (below a certain oxygen threshold O_2^A) and apoptosis, a stochastic phenomenon also regulated by a spread parameter ΔO_2^A. It is defined as:

$$F_{ap}(O_2; O_2^A, \Delta O_2^A) = \frac{1}{2}\left(1 - \tanh\left(\frac{O_2 - O_2^A}{\Delta O_2^A}\right)\right) \tag{12}$$

Finally, oxygen consumption is modelled using a Michaelis-Menten correction F_c, depending on the Michaelis-Menten constant O_2^M [44], as,

$$F_c(O_2; O_2^M) = \frac{O_2}{O_2^M + O_2}. \tag{13}$$

When working with machine learning techniques, using dimensionless variables offers much more robust and generalisable results. Therefore, it is important to carry out a non-dimensionalisation of this mathematical model.

First, the dimensionless variables are defined as:

$$X = \frac{x}{L}, \quad T = \frac{t}{\tau}, \quad N = \frac{C_n}{C_{sat}}, \quad D = \frac{C_d}{C_{sat}}, \quad B = \frac{O_2}{O_2^M}, \tag{14}$$

where L is the size of the microfluidic device and τ is the simulation time.

Eqs. (5)–(7) are therefore reformulated in terms of the dimensionless variables as:

$$\frac{\partial N}{\partial T} = \frac{\partial}{\partial X}\left(D_N \frac{\partial N}{\partial X} - K_N \Pi_{ch}(B;H) F^*_{ch}(N) N \frac{\partial B}{\partial X}\right) + G_N \Pi_{gr}(B;H) F^*_{gr}(N,D) N - G_D F_{ap}(B;A,\Delta A) N, \tag{15}$$

$$\frac{\partial D}{\partial T} = G_D F_{ap}(B;A,\Delta A) N, \tag{16}$$

$$\frac{\partial B}{\partial T} = D_B \frac{\partial^2 B}{\partial X^2} - \alpha_N F^*_c(B) N, \tag{17}$$

with the following dimensionless parameters:

$$D_N = \frac{D_n \tau}{L^2}, \quad K_N = \frac{K_n \tau O_2^M}{L^2}, \quad G_N = \frac{\tau}{\tau_{gr}},$$
$$G_D = \frac{\tau}{\tau_{ap}}, \quad D_B = \frac{D_{O_2}\tau}{L^2}, \quad \alpha_N = \frac{\alpha_n C^M \tau_n}{O_2^M} \tag{18}$$
$$H = \frac{O_2^H}{O_2^M}, \quad A = \frac{O_2^A}{O_2^M}, \quad \Delta A = \frac{\Delta O_2^A}{O_2^M},$$

and the following dimensionless functions:

$$F^*_{ch}(N) = \begin{cases} 1 - N & \text{if} \quad 0 \le N \le 1 \\ 0 & \text{if} \quad N > 1 \end{cases}, \tag{19}$$

$$F^*_{gr}(N,D) = 1 - (N + D), \tag{20}$$

$$F^*_c = \frac{B}{B+1}. \tag{21}$$

Once the model has been established, it is possible to identify the proliferative and migratory features of the cell culture with the model parameters G_N, K_N and H:

- G_N is an indicator of the cell proliferative activity, associated with tumour growth.
- K_N is an indicator of the cell migratory activity, associated with tumour aggressiveness.
- H is a threshold parameter indicating the cell metabolism switch between the proliferative and migratory behaviour, related to the local oxygen level.

2.3. Convolutional neural network set-up and training process

2.3.1. Dataset generation

We used the previously described mathematical model to generate $n = 12000$ virtual results recreating the formation of a necrotic core in a device of $L = 0.2$ cm with a simulation time of $\tau = 3$ days. The mesh element size was $\Delta x = 4 \cdot 10^{-3}$ cm, the time step was $\Delta t = 518$ s, and the initial cell concentration was $C_0 = 4 \cdot 10^7$ cell/mL. The boundary conditions used to simulate this experiment correspond to the consideration of two channels open to continuous medium entrance, as detailed in Ayensa-Jiménez et al. [10]. Briefly, oxygen concentrations at both channels was fixed at 7 mmHg, while full impermeability was assumed for dead cells and Robin boundary conditions for alive cells, with

$$C_n(x=0,L) + J(x=0,L)\left.\frac{\partial C_n}{\partial x}\right|_{x=0,L} = 0. \tag{22}$$

In Eq. (22), $J(x=0, L)$ is a flux control parameter for the boundary at $x = 0$, L, that was adjusted during the fitting process to get optimal values [10], obtaining:

$$\begin{aligned} J(x=0) &= -J = -1{\cdot}10^6 \text{ s/cm}, \\ J(x=L) &= \ \ J = \ \ 1{\cdot}10^6 \text{ s/cm}. \end{aligned} \tag{23}$$

We aim to determine the behaviour of cells in terms of proliferation and migration due to lack of oxygen. This behaviour is determined by the parameters regulating the *go or grow* functions, i.e. G_N, K_N and H, that determine the tumour aggressiveness in response to hypoxia.

The rest of the parameters were considered to have a constant value (shown in Table 1), obtained by substituting in Eq. (18) the fitted value of the parameters given in Ayensa-Jiménez et al. [10].

The values of G_N, K_N and H used for generating the training data were obtained using three independent uniform distributions. Maximum and minimum values for each parameter are detailed in Table 2.

The minimum value for the hypoxia threshold, H, was selected as 0.5 instead of 0 because, in the latter case, cells only proliferate, even when there is a complete lack of oxygen. This is an unrealistic situation, which makes it impossible to appropriately estimate the chemotaxis coefficient.

2.3.2. Convolutional neural network

A Convolutional Neural Network (CNN) was built to predict the three parameters mentioned above from the cell evolution profiles. CNNs have several features of which we can take advantage: i) they are commonly applied to image processing; ii) they are less likely to present overfitting; and, thanks to their structure, iii) they reduce the number of parameters needed, accelerating the training process; and iv) they may infer hierarchical patterns. This is useful when dealing with cell concentration profiles, since the information on model parameters is likely to be locally distributed in them, when using advection-diffusion-reaction equations.

CNNs typically consist of convolutional layers, composed of a number of kernels of a determined size that convolve the input, and pooling layers, which reduce the dimensions of the data. Fully-connected layers are also used to perform the regression or classification tasks. A scheme of the CNN used in the proposed problem is illustrated in Fig. 2. As can be observed, the network receives a two-channel input, corresponding to

Table 1
Values of the constant dimensionless parameters.

Parameter	Value
D_N	0.032
G_D	1.5
D_B	64.8
α_N	5184
A	0.64
ΔA	0.04

Table 2
Range of the dimensionless parameters used in the simulations.

Parameter	G_N	K_N	H
Minimum value	0	0	0.5
Maximum value	0.72	0.243	5.6

both alive and dead cell profiles at the end of the simulation time ($t = \tau = 3$ days), each discretised with 51 points.

In particular, the proposed CNN is composed of four convolutional layers, each followed by batch normalization and average pooling layers. An average pooling layer divides the input into rectangular regions and computes the average value in each region, while batch normalization layers normalize each input channel across a mini-batch. Activation functions are Rectified Linear Units (ReLUs). At the end, there is a fully connected layer, followed by a regression layer, which returns the predicted parameters. A detailed enumeration of all layers is:

1. Convolution Layer: 12 convolutions with kernel size [1,30], stride [1,1] and same padding.
2. Batch normalization with 12 channels.
3. ReLU layer.
4. Average pooling with stride [2,2] and zero padding.
5. Convolution Layer: 32 convolutions with kernel size [1,30], stride [1,1] and same padding.
6. Batch normalization with 32 channels.
7. ReLU layer.
8. Average pooling with stride [2,2] and zero padding.
9. Convolution Layer: 64 convolutions with kernel size [1,30], stride [1,1] and same padding.
10. Batch normalization with 64 channels.
11. ReLU layer.
12. Average pooling with stride [2,2] and zero padding.
13. Convolution Layer: 64 convolutions with kernel size [1,50], stride [1,1] and same padding.
14. Batch normalization with 64 channels.
15. ReLU layer.
16. Fully-connected layer with 3 neurons.
17. Regression Layer.

2.3.3. Training procedure

From the $n = 12000$ virtual results (consisting on cell profiles and *go or grow* parameters) available in the dataset, we used $n_{\text{train}} = 8000$ for training the network, $n_{\text{val}} = 2000$ for validation during the training, and the remaining $n_{\text{test}} = 2000$ for testing the network once trained. The output parameters were normalised in advance.

For the training procedure, we selected the Adam optimiser [39] with a learning rate of $\beta = 1 \cdot 10^{-3}$. Every 20 epochs, the learning rate is decreased by a factor of 0.1 to avoid the stagnation of the loss function. The weights initialisation was performed by means of a Glorot initialiser (also known as Xavier initialiser) [28], while the biases values were initially set to zero.

The training consisted on 50 epochs, with batches of 30 virtual experiments. The loss function is the half-mean-squared-error (HMSE):

$$\text{HMSE} = \frac{1}{2n}\sum_{i=1}^{n}\sum_{j=1}^{3}\left(\hat{y}_j^i - y_j^i\right)^2, \tag{24}$$

where $\hat{y}_j^i$ is the prediction of the jth parameter, corresponding to the ith observation ($i = 1, \ldots, n$, with n the number of data); and y_j^i is the real value.

The CNN model and training procedure were implemented in the Deep Learning Toolbox of Matlab [45].

3. Results

3.1. Network convergence

Fig. 3 shows the evolution of the loss function for both training and test datasets. It can be seen that both decrease as the iterations increase, converging to a low value of the cost function, showing no overfitting.

3.2. Network performance

For each pair of concentration profiles of the test dataset, the network predicts the value of the corresponding parameters, which was then compared to the real one (Fig. 4), showing good agreement for all three parameters. Indeed, the linear correlation coefficient between the real y_i and predicted $\hat{y}_i$ values, ρ, and the Root Mean Squared Error (RMSE),

$$\text{RMSE} = \sqrt{\frac{1}{n}\sum_{i=1}^{n}\left(y_i - \hat{y}_i\right)^2}, \tag{25}$$

were calculated for each parameter, and the corresponding results are shown in Table 3.

As can be seen in Table 3, ρ is above 0.99 in all cases and RMSE is below 0.1, confirming the good results obtained.

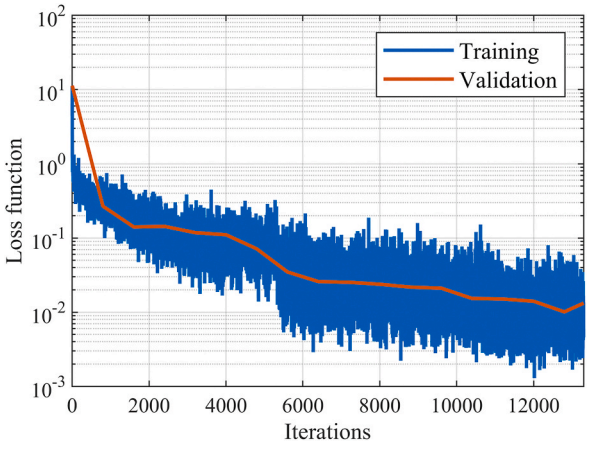

Fig. 3. Network convergence.

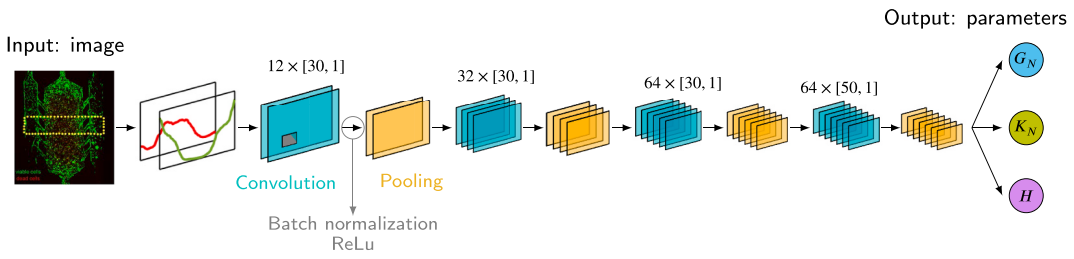

Fig. 2. Convolutional Neural Network scheme.

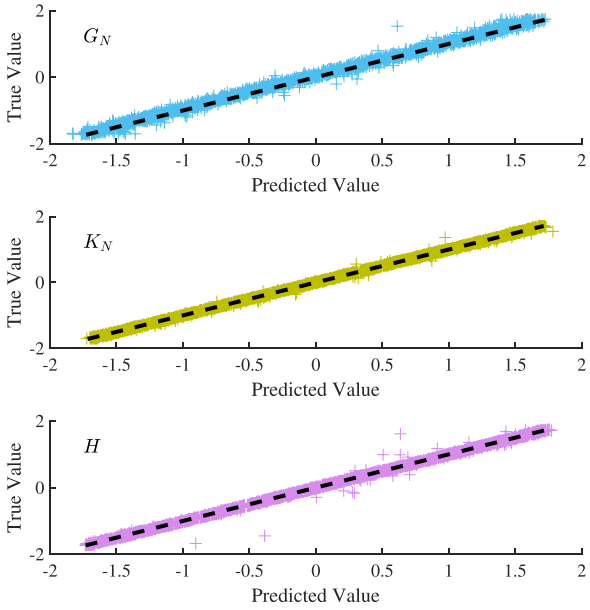

Fig. 4. Predicted vs. real value of the estimated parameters.

Table 3
Correlation coefficient ρ and RMSE for the output parameters.

Parameter	G_N	K_N	H
RMSE	0.0842	0.0270	0.0506
ρ	0.9976	0.9996	0.9987

To illustrate the performance of the network and its sensitivity to noisy input data, virtual profiles with different levels of noise were generated. We added a Gaussian white noise to each cell concentration. More specifically, the input profiles at each point N_j, D_j, with $j = 1, \ldots, 51$ referring to the spatial discretisation nodes, were perturbed using a normal distribution with mean N_j and standard deviation $r \cdot N_j$ where $r \in [0, 1]$ is the noise fraction, in the case of alive cells and proceeding likewise for dead cells. We repeated this procedure for no noise ($r = 0$), a noise level of 1% ($r = 0.01$) and a noise level of 10% ($r = 0.1$). The parameters predicted by the network for each case are shown in Table 4, together with the relative error e in the prediction, calculated as $e = |\widehat{y} - y|/y$.

As expected, the higher the noise level, the higher the relative error. Nevertheless, we used our mathematical model with the predicted parameters to simulate the outcome of the experiment in each of the situations, plotting the results in Fig. 5. The results were able to reproduce the trends of the original data in all cases, showing that our network, despite having been trained with noise-free data, is able to make accurate predictions also for noisy profiles.

3.3. Network soundness

Two different validation procedures were followed to assess the CNN soundness. First, the network convergence soundness (the optimisation algorithm) was tested by changing the weights initialisation, and, second, cross-validation was performed to evaluate the model generalisability.

3.3.1. Network convergence

As commented before, weight initialisation was carried out using a Glorot initialiser, which assigns each weight a value independently sampled from a uniform distribution [28]. Therefore, there is a random component in the initial weights selection, which can influence the results. Nevertheless, if a model is sufficiently good, it is expected that the choice of the initial weights of the CNN layers would not have a significant influence on the results, so that the minimum reached is actually the global one. To test the network soundness regarding this aspect, the CNN was trained with 100 different sets of initial values, randomly selected, and the results were evaluated with the same test dataset.

The boxplot of the RMSE values obtained for each parameter is shown in Fig. 6. The values are small and present small variability, as expected.

3.3.2. Model generalisability

Cross-validation is another test used to assess whether the proposed CNN model is able to generalise. The aim is to prove that the results obtained when predicting values for the test dataset are independent of the dataset used during the training process. We used a k-fold random subsampling cross-validation scheme, represented in Fig. 7, with $k = 10$ iterations. From the considered $n = 12000$ dataset, the test dataset (of size $n_{\text{test}} = 2000$) remained constant throughout the process, so that the results from the different iterations could be objectively compared. In each iteration, the remaining 10000 pieces of data were randomly split into a training dataset (size $n_{\text{train}} = 8000$) and a validation dataset (size $n_{\text{val}} = 2000$). Then, the CNN was trained and its performance was evaluated by predicting the parameters corresponding to the virtual experiments of the training dataset. The RMSE for each parameter was computed at each iteration, and its boxplot is depicted in Fig. 8.

The correlation coefficient ρ was computed for both validation procedures, and its mean for each parameter, together with the corresponding standard error, are shown in Table 5, proving again both the accuracy and the precision of the network.

3.4. Application: predicting the evolution of GBM cultures

In this section, we illustrate the application of the methodology proposed to real images of GBM evolution microfluidic devices. In particular, we use an image of a necrotic core experiment [13], the experiment with which the network has been trained, to predict the parameters; and an image of the pseudopalisade experiment [12] to explore whether the obtained parameters are also valid for other experiments with the same cells. A general scheme of the procedure is depicted in Fig. 9.

The procedure is next explained in more detail. Once the CNN is trained, a real image of the formation of a necrotic core (from Ayuso et al. [13]) is processed using the procedure described in Section 2.1. The resulting cell profiles are non-dimensionalised (dividing the cell profile by C_{sat} and the spatial coordinate by L) and given to the CNN as input. As a result of this process, the CNN predicts the value of the parameters G_N, K_N and H, which determine the tumour behaviour for this particular cell culture (or eventually for a particular patient). The values obtained are $G_N = -0.615$, $K_N = 0.293$ and $H = 2.624$. We can now

Table 4
Predicted values and relative errors for different noise levels.

		Noise level = 0%		Noise level = 1%		Noise level = 10%	
Parameter	True value	Predicted value	Relative error	Predicted value	Relative error	Predicted value	Relative error
G_N	0.3966	0.3764	0.0510	0.3659	0.0775	0.3176	0.1993
K_N	0.1721	0.1720	0.0003	0.1695	0.0150	0.1651	0.0403
H	1.9836	1.9556	0.0141	1.9936	0.0051	2.4866	0.2536

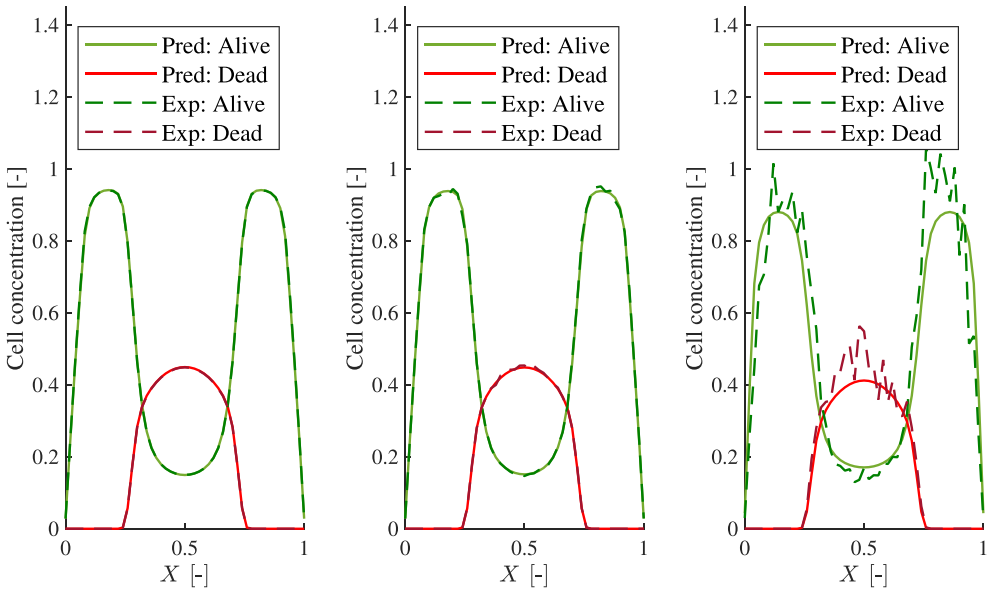

(a) Noise level = 0% (b) Noise level = 1% (c) Noise level = 10%

Fig. 5. Simulations for different noise levels. Predicted (Pred.) data were obtained by means of the mathematical model with the output of the CNN. Experimental (Exp.) data refer to the input profiles given to the CNN for prediction.

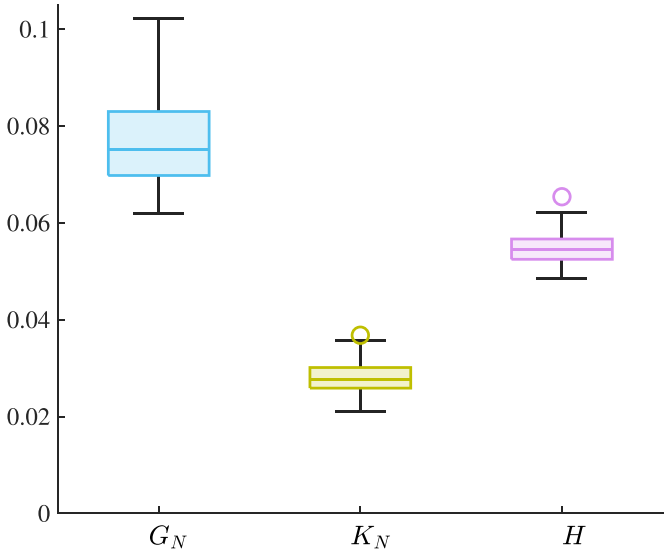

Fig. 6. RMSE box plot for the predicted parameters through 100 different initialisations.

introduce the predicted parameters in our mathematical model and simulate the evolution of the tumour, contrasting the experimental results with the simulated ones. It is worth remarking here that neither the input image nor any similar image has never been seen by the network, which has been trained exclusively with synthetic data. The simulated results, compared to the experimental profiles (input of the CNN) are shown in Fig. 10. Good agreement is shown both for alive and dead cell populations.

Besides, the values obtained from the CNN can be re-dimensionalised (see Eq. (18)) and compared to those fitted with traditional techniques in Ayensa-Jiménez et al. [10]. In Table 6, we compare the values (with dimensions, for easier interpretation) of the grow characteristic time τ_{gr}, the chemotaxis coefficient K_n and the hypoxia threshold O_2^H.

As revealed by Table 6, the values of K_n and O_2^H are fairly similar, but the value of τ_{gr} is completely different. The CNN even predicts a negative value. Despite this fact, the experimental results are well reproduced with the parameters obtained from the CNN (Fig. 10), as they also were with the parameters from Ayensa-Jiménez et al. [10]. This indicates that the behaviour in this experiment is basically migratory, with low effect of the proliferation. To reinforce this hypothesis, a parametric sweep was performed considering 100 necrotic core simulations, varying the values of the rate of proliferation ($1/\tau_{gr}$) following a normal distribution with mean and standard deviation equal to the value fitted in Ayensa-Jiménez et al. [10] ($\mu = \sigma = 1/7.2 \cdot 10^5$ 1/s). The median values of both cell profiles together with their 90% confident intervals are shown in Fig. 12a. These results demonstrate the low influence of the proliferation rate in this particular experimental configuration, even when it reaches negative values. The parametric sweep was repeated for the other two parameters (chemotaxis coefficient and hypoxia threshold), following the same procedure. These parameters clearly have much more influence on the results (Fig. 12c,e).

Finally, we can use these parameters to reproduce other experimental

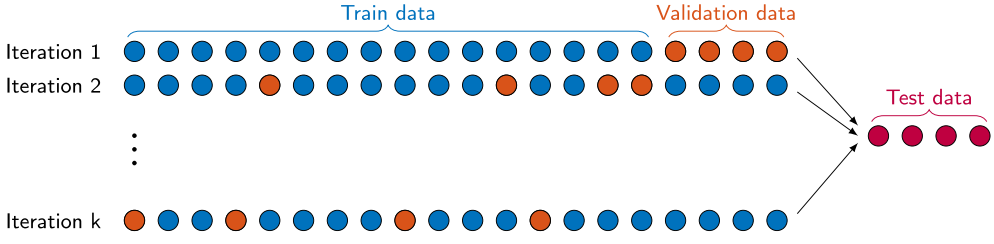

Fig. 7. Repeated random sub-sampling cross-validation scheme.

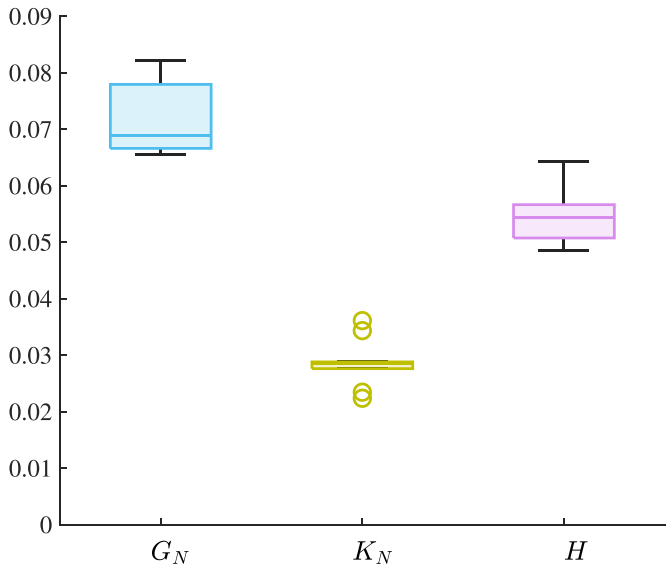

Fig. 8. RMSE box plot for the predicted parameters through the cross-validation.

Table 5
Linear correlation coeficient ρ in both validation procedures (mean ± standard error).

Parameter	G_N	K_N	H
Weight initialisation	0.99743 ± 0.00006	0.99962 ± 0.00001	0.99849 ± 0.00002
Cross validation	0.9978 ± 0.0001	0.99959 ± 0.00004	0.99850 ± 0.00008

results performed with the same U-251 cell line (which is expected to have similar behaviour). In particular, we reproduced the formation of a pseudopalisade (experimental data from Ayuso et al. [12]). In this experiment, the initial cell concentration was lower than in the necrotic core experiment, being $C_0 = 4 \cdot 10^6$ cell/mL. The device's length was $L = 0.0916$ cm and the simulation time was $\tau = 6$ days. Regarding boundary conditions, one of the channels was closed, to simulate an occluded vessel, contrary to what happened in the necrotic core experiment. Thus, in the sealed channel oxygen impermeability was imposed, while in the open one the oxygen concentration was fixed to 2 mmHg. Regarding cell populations, impermeability was assumed for the dead cells and Robin boundary conditions for the alive cells, with $J = 1 \cdot 10^9$ s/cm.

When simulating the experiment with the presented mathematical model, the initial and boundary conditions detailed above and the parameters predicted by the CNN, the obtained results are shown in Fig. 11. Again, good agreement is shown between the experimental and the simulated results. In this case, the behaviour of the cells is also mainly migratory, as the whole chip is under hypoxic conditions (note that both oxygen concentrations in the channels are well below the hypoxia threshold, which is 7 mmHg).

Parametric sweeps were also performed for each of the three parameters as previously explained for the necrotic core experiment. As expected, the rate of proliferation has a minimum influence in the results (Fig. 12b), while both the chemotaxis coefficient and hypoxia threshold significantly influence the resulting cell profiles (Fig. 12d,f). It must be noted that the parametric sweeps related to the pseudopalisade experiment are shown for completeness purposes, as this experiment was not

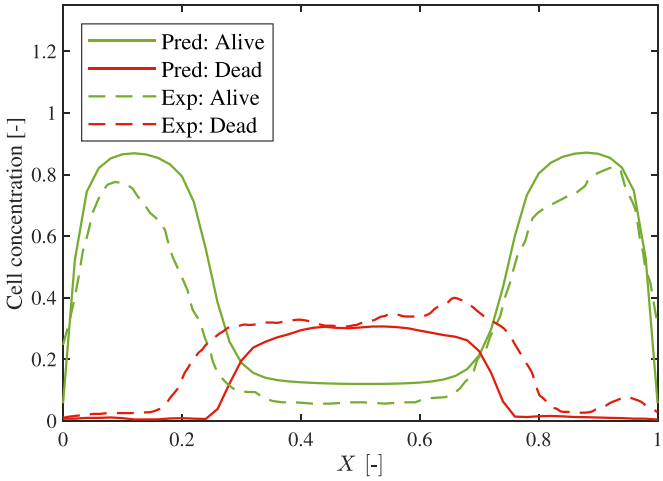

Fig. 10. Simulation of the formation of a necrotic core using the parameters predicted by the CNN from a real image. Predicted (Pred.) data were obtained using the mathematical model with the output of the CNN. Experimental (Exp.) data refers to real experimental data obtained from Ayuso et al. [13].

Table 6
Comparison between parameters obtained from the CNN and fitted with traditional techniques [10].

Parameter	CNN	Literature [10]	Units
τ_{gr}	$-4.2 \cdot 10^5$	$7.2 \cdot 10^5$	s
K_n	$1.8 \cdot 10^{-8}$	$7.5 \cdot 10^{-9}$	cm^2/mmHg ·s
O_2^H	6.6	7.0	mmHg

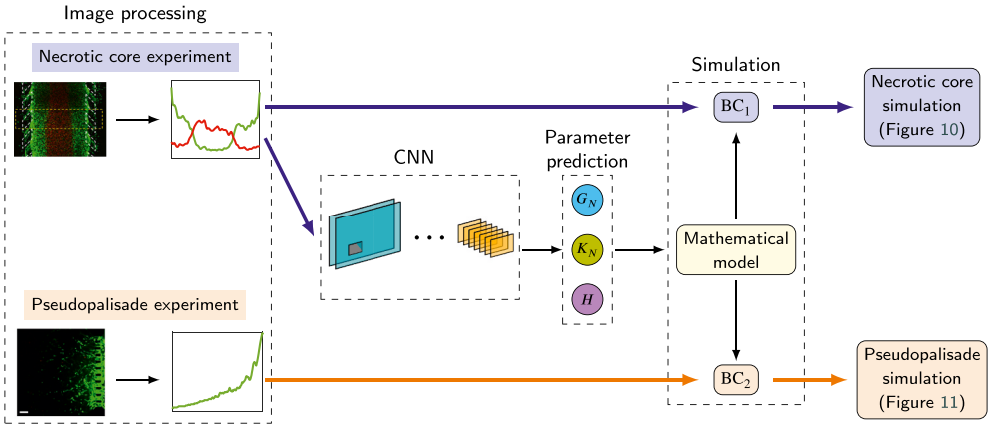

Fig. 9. Procedure followed in the application to real images. BC_1 and BC_2 refer to the different boundary conditions used to simulate the necrotic core and the pseudopalisade experiments, respectively. Fluorescence images from Ayensa-Jiménez et al. [10].

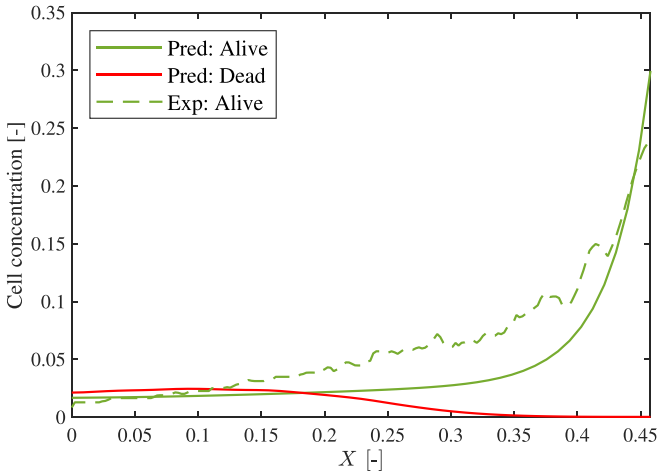

Fig. 11. Simulation of the formation of a pseudopalisade using the parameters predicted by the CNN from a real image. Predicted (Pred.) data were obtained using our mathematical model with the output of the CNN. Experimental (Exp.) data refers to real experimental data obtained from Ayuso et al. [12].

used as input for the CNN. Therefore, the fact that the influence of the rate of proliferation is low in the pseudopalisade experiment does not give any information about the quality of the network performance. It is merely a confirmation that this is also a migratory experiment, thus justifying the use of the network predicted parameters for forecasting.

4. Discussion

The work here presented combines two areas of high research interest nowadays, microfluidics and deep learning. However, according to recent studies [53], the combination of them remains almost unexplored while it offers a great potential and a wide variety of emerging opportunities. In this line, we present an approach for parameter identification from cell culture images using deep learning techniques. Once trained, neural network models are fast to be evaluated, allowing the characterisation of the cell cultures in real-time. When combined with mathematical models, they can be used for forecasting, for evaluating trends and for testing different scenarios, thus enabling efficient decision-making regarding treatment strategies. This real-time evaluation, a characteristic of deep learning models, differentiates this approach from traditional fitting techniques, as once the CNN is trained, predictions can be made for different patients and tumours with no need of performing a costly parametric fitting for each patient and without extra mathematical software solutions.

It should be pointed out that this approach requires the existence of a mathematical model to generate pairs of data and parameters for the Deep Learning training process. However, there exist plenty of validated models, which can support this methodology, not only for GBM evolution [6,21,32,51], but also for other tumours [36]. Consequently, our methodology is only a first step towards a patient-specific tool able to predict, from a cultured patient sample under controlled oxygenation, the parameters determining a particular metabolic switch, such as the *go or grow* behaviour of GBM cultures. This is determinant for the tumour prognosis and response to treatment.

In our case, these three parameters (proliferation rate, chemotaxis coefficient and hypoxia threshold) are part of a mathematical model [10], where the *go or grow* is modelled with two Rectified Linear Unit activation functions (ReLUs). This simulates that cells spend their resources either in proliferating when they have enough oxygen, or in migrating when the conditions are hypoxic, according to the dichotomy reported in GBM literature [32]. Nevertheless, the methodology is limited to learning parameters, and therefore the functional forms of the parametric dependencies must be defined *a priori*. That is, we must take for granted that the behaviour is sufficiently well defined with the two ReLUs already mentioned, or, in general, that the underlying biophysical hypotheses for a

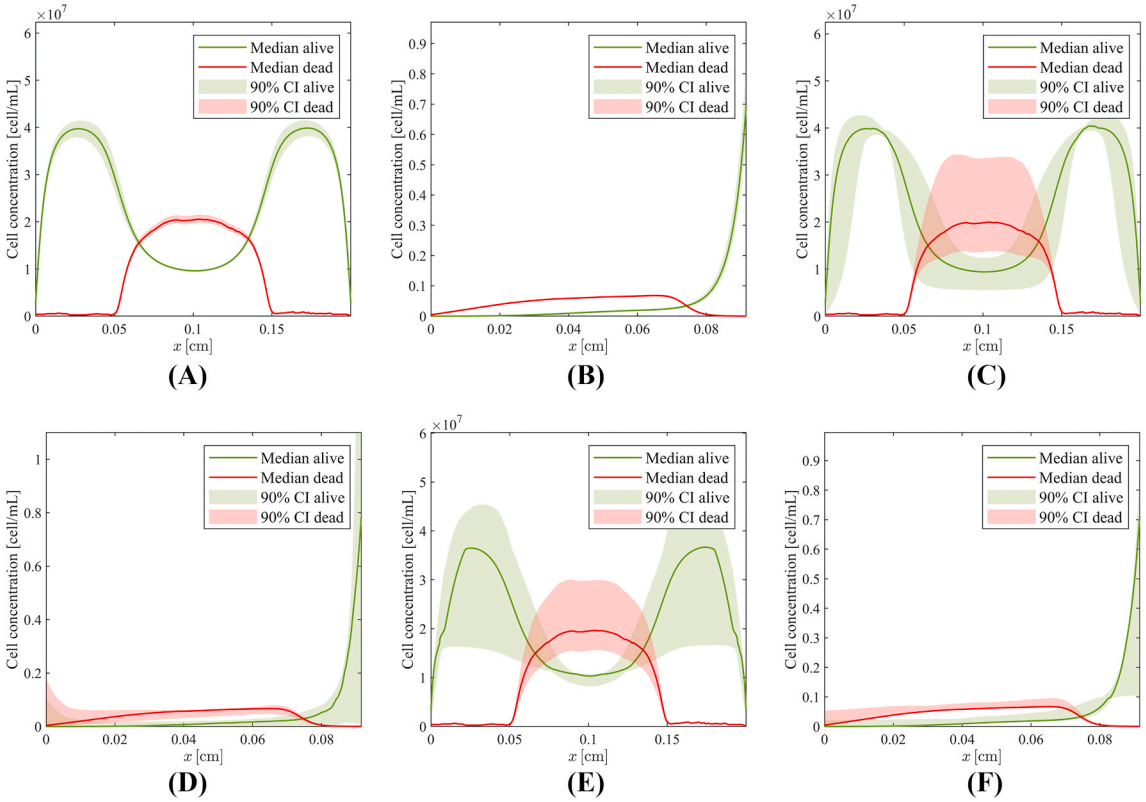

Fig. 12. Median and 90% confident band of results obtained varying each parameter.

particular mechanism and their mathematical description are accurate enough. Even if this is a reasonable assumption, supported by experimental results and previous works, there could exist a better approximation to the *go or grow*, with another parametric dependence, more complex or involving more parameters. Consequently, it would be of great interest to exploit the potential of this combination of deep learning and microfluidic techniques to unravel cell behaviour in a more general way, not limited to the parameters' value. In this line, there are recent works which have introduced physical constraints in the deep learning schemes to give physical meaning to the internal layers [8,9]. These methodologies could be further developed to learn such cell behaviour in a non-parametric way.

Another limitation of the present work is that the CNN is trained with a set of data from a particular experiment (in this case the formation of a necrotic core) with particular boundary and initial conditions. Therefore, it would only be able to predict model parameters from images of this type of experiments, with the prescribed boundary conditions. This implies the need for a good control of the experiment. The benefit is that, once the parameters are obtained, they can be used to simulate the evolution of other similar experiments (as shown in this work for the pseudopalisade experiment).

Regarding the predictive capacity of the network, there is a last issue that has also been illustrated in this work. As shown in Fig. 12a, not every experimental configurations is equally useful for parameter identification, which turns out to be critical when using the parameters for predicting the cell evolution under other experimental set-ups. Indeed, in the presented work, if the values predicted by the network were used in an experiment where proliferation was critical, the results would be misleading. This is not a problem of neither the mathematical model nor the network, but of the selected benchmark experiment, unable to isolate between the different effects and therefore to capture with sufficient accuracy the effect of the growth parameter. This shows the importance of a good design of experiments, isolating the different effects despite the parameter variability and possible correlations [11].

5. Conclusions

Glioblastoma's rapid progression and aggressiveness are triggered by cyclic hypoxia, causing cells to alternate between proliferation and migration depending on the oxygen level (they proliferate above a certain hypoxia threshold and migrate below it). Knowing the precise parameters governing this dichotomous behaviour is of great importance for predicting the response to therapies and the tumour prognosis.

The methodology presented in this paper combines state of the art experimental techniques in cancer research, such as microfluidics, with deep learning techniques (in particular, convolutional neural networks), resulting in a tool able to predict, from a real culture image, the behaviour of the cultured cells in terms of migration and proliferation due to hypoxia. The CNN, trained with synthetic data of the formation of a necrotic core obtained from an experimentally validated mathematical model, shows excellent performance ($\rho > 0.99$ for the three predicted parameters) when used to predict parameters for the test dataset (Fig. 4). The network proves to be sound with respect to convergence (weights initialisation, Fig. 6) and generalisation (cross-validation, Fig. 8). The predicted parameters, which constitute the output of the CNN, can then be introduced in the model to simulate the tumour evolution. Good results have been obtained even for noisy profiles. Although the prediction error increases, the simulation reproduces the experimental trends observed in the formation of a necrotic core, so the network is able to filter the noise to some extent.

Finally, we have tested the CNN for a real application, using a GBM culture image of a necrotic core from a previous experiment of our group. The simulations performed with the prediction's resulting parameters are able to reproduce the experimental results not only for the formation of the necrotic core (Fig. 10), but also for a different experiment, reproducing the formation of a migratory structure called pseudopalisade (Fig. 11). Moreover, the parameters obtained from the network are similar to the ones fitted with the mathematical model using traditional techniques, except for the proliferation rate. Nevertheless, the experimental results are accurately reproduced in the present work, similarly to how they were using conventional fitting techniques. This informs us about the small relevance of proliferation in these experiments, which last few days, are poorly oxygenated and in which the cells show a fundamentally migratory behaviour.

The methodology shown herein combines the increasing power of microfluidic technologies and artificial intelligence tools in order to characterise cell culture behaviour, in what was recently baptized as Intelligent Microfluidics. This new paradigm opens the door to a more quantitative and systematic analysis of cell cultures, enabling a deeper understanding of the different mechanisms involved in tumour progression and, at the same time, glimpsing some directions towards personalized medicine.

Credit authorship contribution statement

Marina Pérez-Aliacar: Methodology, Software, Validation, Formal analysis, Writing - Original Draft, Visualization. **Mohamed H. Doweidar:** Writing - Review & Editing, Resources, Supervision, Project administration, Funding acquisition. **Manuel Doblaré:** Writing - Review & Editing, Resources, Supervision, Project administration, Funding acquisition. **Jacobo Ayensa-Jiménez:** Conceptualization, Methodology, Software, Writing - Original Draft, Writing - Review & Editing, Supervision.

Acknowledgements

The authors gratefully acknowledge the financial support from the Spanish Ministry of Science and Innovation (MICINN), the State Research Agency (AEI), and FEDER, UE through the projects PGC2018-097257-B-C31 and PID2019-106099RB-C44/AEI, the Government of Aragon (DGA) and the Centro de Investigacion Biomedica en Red en Bioingenieria, Biomateriales y Nanomedicina (CIBER-BBN). CIBER-BBN is financed by the Instituto de Salud Carlos III with assistance from the European Regional Development Fund.

References

[1] D.W. Abueidda, M. Almasri, R. Ammourah, U. Ravaioli, I.M. Jasiuk, N.A. Sobh, Prediction and optimization of mechanical properties of composites using convolutional neural networks, Compos. Struct. 227 (2019) 111264.
[2] D.W. Abueidda, S. Koric, N.A. Sobh, H. Sehitoglu, Deep learning for plasticity and thermo-viscoplasticity, Int. J. Plast. 136 (2021) 102852.
[3] M. Al-Haik, H. Garmestani, I.M. Navon, Truncated-Newton training algorithm for neurocomputational viscoplastic model, Comput. Methods Appl. Mech. Eng. 192 (2003) 2249–2267.
[4] M. Al-Haik, M. Hussaini, H. Garmestani, Prediction of nonlinear viscoelastic behavior of polymeric composites using an artificial neural network, Int. J. Plast. 22 (2006) 1367–1392.
[5] B. Alekya, S. Rao, H.J. Pandya, Engineering approaches for characterizing soft tissue mechanical properties: a review, Clin. BioMech. 69 (2019) 127–140.
[6] J. Alfonso, K. Talkenberger, M. Seifert, B. Klink, A. Hawkins-Daarud, K. Swanson, H. Hatzikirou, A. Deutsch, The biology and mathematical modelling of glioma invasion: a review, J. R. Soc. Interface 14 (2017) 20170490.
[7] U. Ali, W. Muhammad, A. Brahme, O. Skiba, K. Inal, Application of artificial neural networks in micromechanics for polycrystalline metals, Int. J. Plast. 120 (2019) 205–219.
[8] J. Ayensa-Jiménez, M.H. Doweidar, J.A. Sanz-Herrera, M. Doblaré, On the Application of Physically-Guided Neural Networks with Internal Variables to Continuum Problems, 2020 arXiv preprint arXiv:2011.11376.
[9] J. Ayensa-Jiménez, M.H. Doweidar, J.A. Sanz-Herrera, M. Doblaré, Prediction and identification of physical systems by means of physically-guided neural networks with meaningful internal layers, Comput. Methods Appl. Mech. Eng. 381 (2021) 113816.
[10] J. Ayensa-Jiménez, M. Pérez-Aliacar, T. Randelovic, S. Oliván, L. Fernández, J. A. Sanz-Herrera, I. Ochoa, M.H. Doweidar, M. Doblaré, Mathematical formulation and parametric analysis of in vitro cell models in microfluidic devices: application to different stages of glioblastoma evolution, Sci. Rep. 10 (2020) 1–21.
[11] J. Ayensa-Jiménez, M. Pérez-Aliacar, T. Randelovic, J.A. Sanz-Herrera, M. H. Doweidar, M. Doblaré, Analysis of the parametric correlation in mathematical modeling of in vitro glioblastoma evolution using copulas, Mathematics 9 (2021) 27.

[12] J.M. Ayuso, R. Monge, A. Martínez-González, M. Virumbrales-Muñoz, G. A. Llamazares, J. Berganzo, A. Hernández-Laín, J. Santolaria, M. Doblaré, C. Hubert, et al., Glioblastoma on a microfluidic chip: generating pseudopalisades and enhancing aggressiveness through blood vessel obstruction events, Neuro Oncol. 19 (2017) 503–513.

[13] J.M. Ayuso, M. Virumbrales-Muñoz, A. Lacueva, P.M. Lanuza, E. Checa-Chavarria, P. Botella, E. Fernández, M. Doblare, S.J. Allison, R.M. Phillips, et al., Development and characterization of a microfluidic model of the tumour microenvironment, Sci. Rep. 6 (2016) 1–16.

[14] D.J. Brat, Glioblastoma: biology, genetics, and behavior, Am. Soc.Clin. Oncol.Educ. Book 32 (2012) 102–107.

[15] D.J. Brat, E.G. Van Meir, Vaso-occlusive and prothrombotic mechanisms associated with tumor hypoxia, necrosis, and accelerated growth in glioblastoma, Lab. Invest. 84 (2004) 397.

[16] D. Bray, Cell movements: from molecules to motility, Garland Science (2000).

[17] I. Cabeza-Gil, I. Ríos-Ruiz, B. Calvo, Customised selection of the haptic design in c-loop intraocular lenses based on deep learning, Ann. Biomed. Eng. 48 (2020) 2988–3002.

[18] F. Caschera, M.A. Bedau, A. Buchanan, J. Cawse, D. de Lucrezia, G. Gazzola, M. M. Hanczyc, N.H. Packard, Coping with complexity: machine learning optimization of cell-free protein synthesis, Biotechnol. Bioeng. 108 (2011) 2218–2228.

[19] M. Cilla, I. Pérez-Rey, M.A. Martínez, E. Peña, J. Martínez, On the use of machine learning techniques for the mechanical characterization of soft biological tissues, Int. J. Numer. Methods Biomed. Eng. 34 (2018), e3121.

[20] M.L. Coluccio, G. Perozziello, N. Malara, E. Parrotta, P. Zhang, F. Gentile, T. Limongi, P.M. Raj, G. Cuda, P. Candeloro, et al., Microfluidic platforms for cell cultures and investigations, Microelectron. Eng. 208 (2019) 14–28.

[21] M. Conte, S. Casas-Tintò, J. Soler, Modeling invasion patterns in the glioblastoma battlefield, PLoS Comput. Biol. 17 (2021), e1008632.

[22] G. Ellis, C. Yao, R. Zhao, D. Penumadu, Stress-strain modeling of sands using artificial neural networks, J. Geotech. Eng 121 (1995) 429–435.

[23] D. Friedmann-Morvinski, Glioblastoma heterogeneity and cancer cell plasticity, Crit. Rev. Oncog. 19 (2014).

[24] F.B. Furnari, T. Fenton, R.M. Bachoo, A. Mukasa, J.M. Stommel, A. Stegh, W. C. Hahn, K.L. Ligon, D.N. Louis, C. Brennan, et al., Malignant astrocytic glioma: genetics, biology, and paths to treatment, Gene Dev. 21 (2007) 2683–2710.

[25] T. Furukawa, G. Yagawa, Implicit constitutive modelling for viscoplasticity using neural networks, Int. J. Numer. Methods Eng. 43 (1998) 195–219.

[26] E.A. Galan, H. Zhao, X. Wang, Q. Dai, W.T. Huck, S. Ma, Intelligent microfluidics: the convergence of machine learning and microfluidics in materials science and biomedicine, Matter 3 (2020) 1893–1922.

[27] J. Ghaboussi, D. Sidarta, New nested adaptive neural networks (nann) for constitutive modeling, Comput. Geotech. 22 (1998) 29–52.

[28] X. Glorot, Y. Bengio, Understanding the difficulty of training deep feedforward neural networks, in: Proceedings of the Thirteenth International Conference on Artificial Intelligence and Statistics, JMLR Workshop and Conference Proceedings, 2010, pp. 249–256.

[29] D.J. Guckenberger, T.E. de Groot, A.M. Wan, D.J. Beebe, E.W. Young, Micromilling: a method for ultra-rapid prototyping of plastic microfluidic devices, Lab Chip 15 (2015) 2364–2378.

[30] E. Halilaj, A. Rajagopal, M. Fiterau, J.L. Hicks, T.J. Hastie, S.L. Delp, Machine learning in human movement biomechanics: best practices, common pitfalls, and new opportunities, J. Biomech. 81 (2018) 1–11.

[31] H. Hatzikirou, D. Basanta, M. Simon, K. Schaller, A. Deutsch, 'go or grow': the key to the emergence of invasion in tumour progression? Math. Med. Biol.: a journal of the IMA 29 (2012) 49–65.

[32] H. Hatzikirou, A. Deutsch, C. Schaller, M. Simon, K. Swanson, Mathematical modelling of glioblastoma tumour development: a review, Math. Model Methods Appl. Sci. 15 (2005) 1779–1794.

[33] S. Helgadottir, B. Midtvedt, J. Pineda, A. Sabirsh, C.B. Adiels, S. Romeo, D. Midtvedt, G. Volpe, Extracting Quantitative Biological Information from Brightfield Cell Images Using Deep Learning, 2020 arXiv preprint arXiv: 2012.12986.

[34] M.P. Hosseini, A. Hosseini, K. Ahi, A review on machine learning for eeg signal processing in bioengineering, IEEE .Rev. Biomed. Eng. (2020).

[35] A. Isozaki, J. Harmon, Y. Zhou, S. Li, Y. Nakagawa, M. Hayashi, H. Mikami, C. Lei, K. Goda, Ai on a chip, Lab Chip 20 (2020) 3074–3090.

[36] A.M. Jarrett, E.A. Lima, D.A. Hormuth, M.T. McKenna, X. Feng, D.A. Ekrut, A.C. M. Resende, A. Brock, T.E. Yankeelov, Mathematical models of tumor cell proliferation: a review of the literature, Expet Rev. Anticancer Ther. 18 (2018) 1271–1286.

[37] S. Jung, J. Ghaboussi, Neural network constitutive model for rate-dependent materials, Comput. Struct. 84 (2006) 955–963.

[38] A. Kathagen-Buhmann, A. Schulte, J. Weller, M. Holz, C. Herold-Mende, R. Glass, K. Lamszus, Glycolysis and the pentose phosphate pathway are differentially associated with the dichotomous regulation of glioblastoma cell migration versus proliferation, Neuro Oncol. 18 (2016) 1219–1229.

[39] D.P. Kingma, J. Ba, Adam: A Method for Stochastic Optimization, 2014 arXiv preprint arXiv:1412.6980.

[40] G. Litjens, T. Kooi, B.E. Bejnordi, A.A.A. Setio, F. Ciompi, M. Ghafoorian, J.A. Van Der Laak, B. Van Ginneken, C.I. Sánchez, A survey on deep learning in medical image analysis, Med. Image Anal. 42 (2017) 60–88.

[41] M. Liu, L. Liang, W. Sun, Estimation of in vivo constitutive parameters of the aortic wall using a machine learning approach, Comput. Methods Appl. Mech. Eng. 347 (2019) 201–217.

[42] A. Mangal, E.A. Holm, Applied machine learning to predict stress hotspots i: face centered cubic materials, Int. J. Plast. 111 (2018) 122–134.

[43] A. Mangal, E.A. Holm, Applied machine learning to predict stress hotspots ii: hexagonal close packed materials, Int. J. Plast. 114 (2019) 1–14.

[44] A. Martínez-González, G.F. Calvo, L.A.P. Romasanta, V.M. Pérez-García, Hypoxic cell waves around necrotic cores in glioblastoma: a biomathematical model and its therapeutic implications, Bull. Math. Biol. 74 (2012) 2875–2896.

[45] MATLAB Deep Learning Toolbox, Version R2020b. Matlab Deep Learning Toolbox. The MathWorks, Natick, MA, USA.

[46] B. Mosadegh, W. Saadi, S.J. Wang, N.L. Jeon, Epidermal growth factor promotes breast cancer cell chemotaxis in cxcl12 gradients, Biotechnol. Bioeng. 100 (2008) 1205–1213.

[47] T. Oike, Y. Suzuki, K.i. Sugawara, K. Shirai, S.e. Noda, T. Tamaki, M. Nagaishi, H. Yokoo, Y. Nakazato, T. Nakano, Radiotherapy plus concomitant adjuvant temozolomide for glioblastoma: Japanese mono-institutional results, PloS One 8 (2013), e78943.

[48] Q.T. Ostrom, H. Gittleman, P. Farah, A. Ondracek, Y. Chen, Y. Wolinsky, N. E. Stroup, C. Kruchko, J.S. Barnholtz-Sloan, Cbtrus statistical report: primary brain and central nervous system tumors diagnosed in the United States in 2006-2010, Neuro Oncol. 15 (2013) ii1–ii56.

[49] M. Pfeiffer, C. Riediger, J. Weitz, S. Speidel, Learning soft tissue behavior of organs for surgical navigation with convolutional neural networks, Int. J. Comput.Assist. Radiol.Surg 14 (2019) 1147–1155.

[50] R. Phellan, B. Hachem, J. Clin, J.M. Mac-Thiong, L. Duong, Real-time biomechanics using the finite element method and machine learning: review and perspective, Med. Phys. 48 (2021) 7–18.

[51] M. Protopapa, A. Zygogianni, G.S. Stamatakos, C. Antypas, C. Armpilia, N. K. Uzunoglu, V. Kouloulias, Clinical implications of in silico mathematical modeling for glioblastoma: a critical review, Journal of neuro-oncology 136 (2018) 1–11.

[52] M.I. Razzak, S. Naz, A. Zaib, Deep learning for medical image processing: overview, challenges and the future, Classification in BioApps (2018) 323–350.

[53] J. Riordon, D. Sovilj, S. Sanner, D. Sinton, E.W. Young, Deep learning with microfluidics for biotechnology, Trends Biotechnol. 37 (2019) 310–324.

[54] E.K. Sackmann, A.L. Fulton, D.J. Beebe, The present and future role of microfluidics in biomedical research, Nature 507 (2014) 181–189.

[55] C. Settgast, G. Hütter, M. Kuna, M. Abendroth, A hybrid approach to simulate the homogenized irreversible elastic–plastic deformations and damage of foams by neural networks, Int. J. Plast. 126 (2020) 102624.

[56] D. Shen, G. Wu, H.I. Suk, Deep learning in medical image analysis, Annu. Rev. Biomed. Eng. 19 (2017) 221–248.

[57] Y. Shin, S. Han, J.S. Jeon, K. Yamamoto, I.K. Zervantonakis, R. Sudo, R.D. Kamm, S. Chung, Microfluidic assay for simultaneous culture of multiple cell types on surfaces or within hydrogels, Nat. Protoc. 7 (2012) 1247–1259.

[58] D.E. Sidarta, Neural Network-Based Constitutive Modeling of Granular Material, 2001.

[59] Z. Tatárová, J. Abbuehl, S. Maerkl, J. Huelsken, Microfluidic co-culture platform to quantify chemotaxis of primary stem cells, Lab Chip 16 (2016) 1934–1945.

[60] G.H. Teichert, A. Natarajan, A. Van der Ven, K. Garikipati, Machine learning materials physics: integrable deep neural networks enable scale bridging by learning free energy functions, Comput. Methods Appl. Mech. Eng. 353 (2019) 201–216.

[61] J.F. Unger, C. Könke, Neural networks as material models within a multiscale approach, Comput. Struct. 87 (2009) 1177–1186.

[62] Q. Xie, S. Mittal, M.E. Berens, Targeting adaptive glioblastoma: an overview of proliferation and invasion, Neuro Oncol. 16 (2014) 1575–1584.

[63] K. Yao, N.D. Rochman, S.X. Sun, Cell type classification and unsupervised morphological phenotyping from low-resolution images using deep learning, Sci. Rep. 9 (2019) 1–13.

[64] N. Zhang, S.L. Shen, A. Zhou, Y.F. Jin, Application of lstm approach for modelling stress–strain behaviour of soil, Appl. Soft Comput. 100 (2021) 106959.